


Atom Pairing in Optical Superlattices

J. Kangara,¹ Chingyun Cheng,^{1,2} S. Pegahan,¹ I. Arakelyan,¹ and J. E. Thomas^{1,*}

¹*Department of Physics, North Carolina State University, Raleigh, North Carolina 27695, USA*

²*Department of Physics, Duke University, Durham, North Carolina 27708, USA*

 (Received 22 September 2017; revised manuscript received 5 December 2017; published 21 February 2018)

We study the pairing of fermions in a one-dimensional lattice of tunable double-well potentials using radio-frequency spectroscopy. The spectra reveal the coexistence of two types of atom pairs with different symmetries. Our measurements are in excellent quantitative agreement with a theoretical model, obtained by extending the Green's function method of Orso *et al.* [*Phys. Rev. Lett.* **95**, 060402 (2005)] to a bichromatic 1D lattice with nonzero harmonic radial confinement. The predicted spectra comprise hundreds of discrete transitions, with symmetry-dependent initial state populations and transition strengths. Our work provides an understanding of the elementary pairing states in a superlattice, paving the way for new studies of strongly interacting many-body systems.

DOI: 10.1103/PhysRevLett.120.083203

Optical superlattices, comprising two optical standing waves with a tunable relative phase, enable wide control of the band structure of ultracold atomic gases. Ground breaking experiments with bosonic atoms in superlattices have simulated Dirac dynamics, such as Klein tunneling [1,2], by producing linear dispersion. A relative phase near zero creates periodic double-well potentials with controllable asymmetry. Single atoms in the right or left states of tilted double-well potentials have been employed to study nonequilibrium dynamics [3] and to provide an effective spin-orbit interaction with negligible optical scattering [4]. This has enabled the observation of antiferromagnetic spin textures [4]. Cyclic variation of the phase and corresponding double-well symmetry has been used to observe topological (Thouless) pumping for weakly interacting bosons [5] and fermions [6]. Harmonic confinement with an applied spin-dependent force produces a bilayer system, with geometric control of pairing interactions between species in separated layers [7]. Anharmonicity in optical lattice potentials generally entangles the center of mass and relative coordinates of confinement-induced atom pairs, modifying the pair binding energy as predicted theoretically [8] and observed in experiments [9]. Anharmonic coupling also causes confinement-induced loss resonances, which have been observed [10,11] and studied theoretically (see [12] and references therein), and is predicted to modify confinement-induced states in a deep double-well potential [13]. With magnetically tunable two-body interactions and wide control of the dispersion relation, ultracold atomic gases in superlattices provide a broad platform for studies of many-body physics, including entanglement, nonequilibrium dynamics, and exotic new states of matter. However, there has been no quantitative study of the elementary atom pairing states in a superlattice.

In this Letter, we report precision measurements of radio-frequency spectra for a 50-50 mixture of the two lowest hyperfine states (denoted $|1\rangle$, $|2\rangle$) of fermionic ${}^6\text{Li}$ atoms in an optical superlattice, comprising attractive (red) and repulsive (green) standing waves with an adjustable relative phase. The trapped cloud is magnetically tuned near the broad collisional (Feshbach) resonance at 832.2 G [14,15] to control the s -wave scattering length a_{12} . The observed spectra exhibit a rich relative-phase-dependent structure, which we explain quantitatively using a beyond Hubbard model treatment, implemented by extending the rigorous Green's function method of Orso *et al.* [8] to a 1D superlattice with nonzero harmonic radial confinement.

The bichromatic superlattice potential (Fig. 1) is created by combining on a beam splitter two optical fields of wavelengths $\lambda_1 = 1064$ nm and $\lambda_2 = 532$ nm, with the

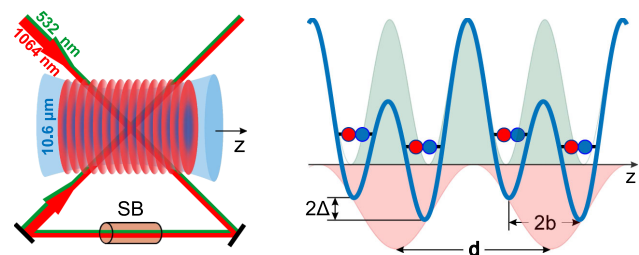


FIG. 1. A 1D optical superlattice, formed by crossed 1064/532 nm laser beams, traps atoms along the z axis, while a $10.6\ \mu\text{m}$ CO_2 laser provides radial confinement. The potential energy for the lattice of double wells is given by Eq. (1) with d the period and ϕ the relative phase set by a Soleil-Babinet compensator (SB), which determines the separation $2b$ and a tilt 2Δ between the double-well minima. In the double-well potentials, atoms form two types of pairs with similar total energies, which can be thermally populated and probed by radio-frequency spectroscopy.

second field obtained by frequency doubling of the first. The intensities of the two beams are controlled by acousto-optic modulators, with the green modulator operating at precisely twice the frequency of the red. The combined beams are split into two beam pairs, which intersect at an angle $\theta = 91.0^\circ$ to create a fundamental lattice, denoted “red,” with a period $d = \lambda_1/[2 \sin(\theta/2)] = 0.75 \mu\text{m}$ and a secondary lattice, denoted “green,” with period $d/2$. The relative phase ϕ between the standing waves is manually tunable using a calibrated Soleil-Babinet compensator [16] placed in the path of the second beam pair to control the symmetry of the periodic double-well potential,

$$V(z_1) = -s_1 E_R \cos^2(kz_1) + s_2 E_R \cos^2(2kz_1 + \phi/2), \quad (1)$$

where $k = \pi/d$ and $E_R = \hbar^2 k^2 / (2m) = h \times 14.9 \text{ kHz}$ is the recoil energy. A CO_2 laser trap propagating along the z axis provides additional radial confinement. Then, $V(x_1, y_1) = m\omega_\perp^2 (x_1^2 + y_1^2)/2$, with $\omega_\perp = 2\pi \times \beta E_R / h$ as the net radial frequency and $\beta = 0.0166$. Red and green lattice depths s_1 and s_2 are calibrated by modulation of the lattice amplitudes to induce interband transitions [16]. For our experiments $s_1 = 7.0$ and $s_2 = 16.5$. The trapped cloud is typically $\simeq 30 \mu\text{m}$ in length, corresponding to $\simeq 40$ sites, with 250 atoms per site.

The atoms are cooled by evaporation near 832 G and loaded into the red lattice by increasing the intensity of the 1064 nm laser beam over 250 ms, at fixed CO_2 laser trap intensity. After raising the red lattice to the desired depth, the CO_2 laser trap is increased to provide additional radial confinement as the repulsive green lattice is ramped up over 250 ms. While the atoms are being loaded into the superlattice, the bias magnetic field is tuned to set the desired scattering length. A radio-frequency pulse of duration $\tau = 20 \text{ ms}$ is then applied, inducing a transition from a hyperfine state $|2\rangle$ to an initially unoccupied state $|3\rangle$. We measure the fraction of atoms lost from state $|2\rangle$ versus radio frequency ν .

Spectra measured at 800.6 G probe all of the transitions from initially occupied $|12\rangle$ atom pair states with $d/a_{12} = +1.28$. The final states are $|13\rangle$ atom pair states, where $d/a_{13} = -3.78$. For data taken in the nearly symmetric double-well configuration, $\phi \simeq 0$, we expect that two-atom states in the first and second bands will be close in energy and thermally occupied, as the single particle states are the nearly degenerate symmetric and antisymmetric states of a double-well potential, $\varphi_\pm(z_1) \simeq [\varphi_0(z_1 - b) \pm \varphi_0(z_1 + b)]/\sqrt{2}$, where $\varphi_0(z_1)$ is a ground harmonic oscillator state and $2b \simeq 0.466d$ is the separation between the double-well minima. Shifting ϕ slightly away from zero localizes the center of mass in either the right or left well, strongly modifying the excitation spectra by breaking the symmetry and increasing the initial state energy separation.

To understand the origin of the spectra, we begin by determining the bound eigenstates and corresponding

energies for two interacting atoms in a one-dimensional bichromatic superlattice with harmonic radial confinement. We employ a multiband model, which is summarized briefly here and described in detail in the Supplemental Material [16]. Our model is based on the Green’s function method of Ref. [8], which treated the single 1D lattice case with no radial confinement. For harmonic radial confinement, the center of mass (c.m.) X, Y motion is independent of the internal state, so we need only the energies E and eigenstates for the coupled relative $\mathbf{r} \equiv (x, y, z)$ and c.m. Z motion of the two atoms. The relevant Hamiltonian is

$$H(\mathbf{r}, Z) = H^0(\mathbf{r}, Z) + g\delta(\mathbf{r}) \frac{\partial}{\partial r} [r \dots], \quad (2)$$

where $g = 4\pi\hbar^2 a_{12}/m$ [21] and

$$H^0(\mathbf{r}, Z) = -\frac{\hbar^2}{2\mu} \nabla_{\mathbf{r}}^2 + \frac{1}{2} \mu \omega_\perp^2 r_\perp^2 - \frac{\hbar^2}{2M} \frac{\partial^2}{\partial Z^2} + U(Z, z), \quad (3)$$

with $\mu = m/2$, $M = 2m$, and m as the atom mass. Here, $r_\perp^2 = x^2 + y^2$ and $U(Z, z) = V(Z + z/2) + V(Z - z/2)$.

The bound state wave functions for an atom pair of energy E and quasimomentum Q take the form

$$\Psi_E(\mathbf{r}, Z) \propto \int dZ' G_E^s(\mathbf{r}, Z; 0, Z') f_E^Q(Z'), \quad (4)$$

where G_E^s is a Green’s function, which we expand in a product basis comprising radial harmonic oscillator states and single particle Bloch states for lattice parameters $s \equiv (s_1, s_2, \phi)$. The function $f_E^Q(Z)$ is determined by solving an eigenvalue equation [16]. Using a nine-band model and 20 lattice sites, we obtain for each chosen E and Q nine solutions $f_E^Q(Z)$ and corresponding d/a values, arising from different combinations of c.m. and binding energy with the same total E and Q . We order the solutions by their d/a values, from most negative to most positive.

We note that $f_E^Q(Z)$ is not the c.m. state, as $\Psi_E(\mathbf{r}, Z)$ generally does not factor, entangling the atom pair relative coordinate \mathbf{r} and the c.m. Z coordinate. However, the Franck-Condon factors for the transitions are proportional to the square of the overlap integrals of the $f_E^Q(Z)$ functions for the initial and final states [16], which provides substantial insight.

Figures 2(a) and 2(d) show the two lowest d/a solutions for a variety of energies E , as green and blue dots at low resolution [16] and as continuous curves at high resolution (insets). Note that the change in color from left to right is a result of our d/a labeling: for the same E , the smallest (leftmost) d/a solutions are green; the next larger d/a solutions are blue. For simplicity, we show predictions for $Q = 0$, as the Q dependence for our lattice parameters is relatively small [16]. States A and B are the two bound states of lowest total energy at $d/a_{12} = 1.28$, denoted by the

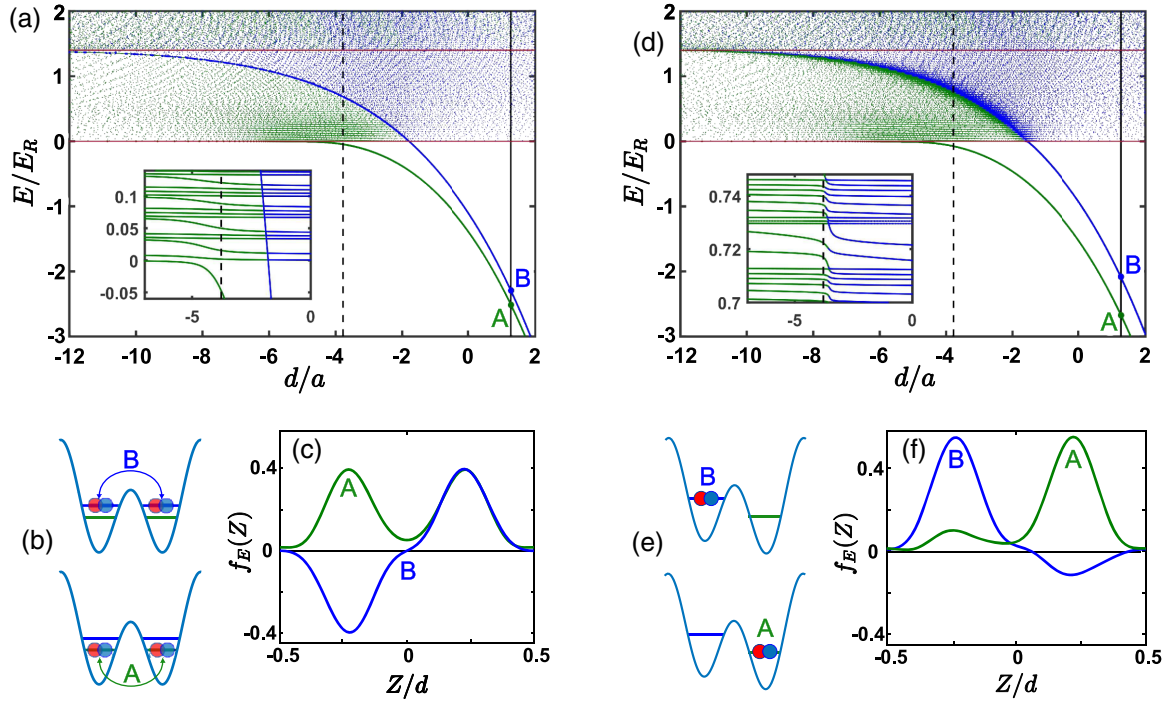


FIG. 2. Dimer energies E for a lattice of double-well potentials versus d/a . For each E , green and blue denote the two smallest d/a values. A and B show the initially populated $|12\rangle$ dimer states with $d/a_{12} = 1.28$. Crossings with the dashed black line at $d/a_{13} = -3.78$ determine final $|13\rangle$ dimer states. The red horizontal lines denote the lowest energy for two noninteracting atoms in the first band (lower red line) and for one in each of the first two bands (upper red line). (a) Energy diagram for symmetric double wells, $\phi = 0$; (b) Illustrations depict delocalized A and B dimer states. (c) Corresponding eigenstates $f_E(Z)$ [see Eq. (4)] versus c.m. coordinate Z are A symmetric or B antisymmetric with respect to the site center. (d) Energy diagram for tilted double wells, $\phi = \pi/35$; (e) Illustrations depict localized right (A) or left (B) dimer states. (f) Corresponding $f_E(Z)$. Insets show typical structure for states above $E = 0$.

vertical solid black line. For symmetric double-well potentials with $\phi = 0$ and $Q = 0$, dimer states A and B are delocalized between the right and left wells, respectively, as depicted in Fig. 2(b) and are symmetric or antisymmetric in the c.m. Z coordinate relative to the double-well center, as shown by the eigenstates $f_E^Q(Z)$ of Fig. 2(c). For tilted double-well potentials with $\phi = \pi/35$, states A and B are localized in the right or left well [Fig. 2(e)], breaking symmetry [Fig. 2(f)] and increasing the $A - B$ energy separation compared to Fig. 2(a). The green E versus d/a solid curve originating at state A asymptotes to the lowest energy of two unbound atoms in the first band, $2E_{q_1=0}^1 \equiv 0$ (lower red horizontal line). The blue curve originating at state B asymptotes to the lowest energy for two unbound atoms, one in each of the first and second bands, $E_{\pm 1}^2 + E_{\mp 1}^1 - 2E_0^1$ (upper red horizontal line).

The insets of Figs. 2(a) and 2(d), for energies $E > 0$, show structure similar to states studied theoretically for three-dimensional harmonic confinement [22,23]. Here, the coarse structure arises from the radial energy spacing $2\beta = 0.033E_R$, while the finer structure arises from the lattice energy spacing, which depends on the number of sites: 20 for the model shown here [16]. For $\phi = 0$ and $Q = 0$, the blue curve starting at B in Fig. 2(a), which arises

from odd symmetry dimer states, crosses several nominally horizontal green and blue curves, which arise from even symmetry states. In contrast, for $\phi \neq 0$, the tilted potential breaks symmetry and strongly mixes the two lowest lattice states, which have opposite symmetry. For $E > 0$, this mixing changes the crossings of the blue curve in Fig. 2(a) to avoided crossings in Fig. 2(d), blurring the energy diagram.

To obtain the spectrum for $|12\rangle \rightarrow |13\rangle$ radio-frequency transitions, we determine the possible resonance frequencies from the energies E_i of the initial pair states, where $d/a_{12} = 1.28$, and the energies E_f of the final pair states, where $d/a_{13} = -3.78$. The corresponding transition strengths are computed from the overlap integrals of the normalized two-atom eigenstates $\langle f|i\rangle$. For transitions originating in dimer state $i = A$ or B , we compute the normalized spectrum,

$$S_i(\nu) = \frac{1}{\pi} \sum_f \frac{\gamma |\langle f|i\rangle|^2}{[\nu - (E_f - E_i)/\hbar]^2 + \gamma^2}, \quad (5)$$

where ν is the radio frequency relative to the resonance frequency of the bare atom $2 \rightarrow 3$ transition. γ denotes the spectral linewidth (HWHM) $\simeq 1.8$ kHz, which is small

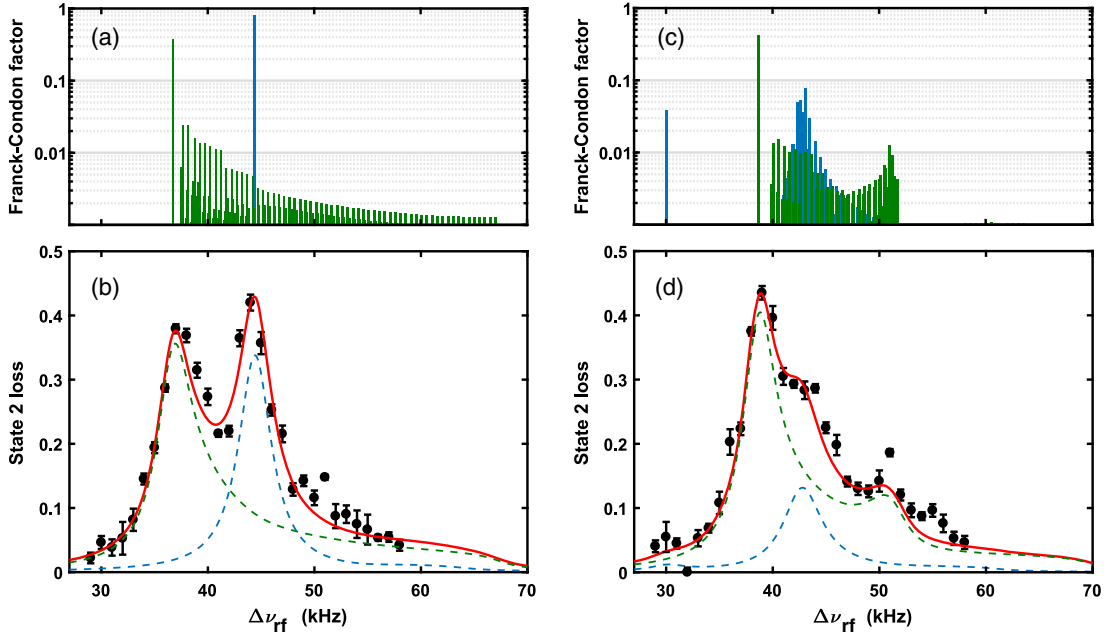


FIG. 3. Radio-frequency $|12\rangle \rightarrow |13\rangle$ dimer transition spectra (black dots) versus predictions (red curves). Green and blue denote contributions from states A and B of Fig. 2. (a) Calculated Franck-Condon factors (log scale) for symmetric double-well potentials, $\phi = 0$ as a function of transition frequency. (b) Measured spectrum showing transitions from the symmetric (A) and antisymmetric (B) states. (c) Calculated Franck-Condon factors for tilted double-well potentials, $\phi = \pi/35$. (d) Measured spectrum showing transitions from the localized right (A) and localized left (B) states of Fig. 2(d). Error bars denote the standard deviation of the mean of five runs.

compared to $(E_f - E_i)/h$ and comparable to that of our previous measurements [24].

The top panels of Figs. 3(a) and 3(c) show the Franck-Condon factors $|\langle f|i\rangle|^2$ versus transition frequency, for transitions from the initial bound states $i = A, B$ of Figs. 2(a) and 2(d), respectively, to final bound states f with a fixed value of $d/a_{13} = -3.78$. For $\phi = 0$, transitions from the tightly bound symmetric state A (green) comprise a dominant excitation to the lowest-lying, most tightly bound symmetric state (left peak) and to a weaker quasicontinuum of excited bound states. The latter corresponds to a threshold spectrum for $\beta \rightarrow 0$ [25]. For $\phi = 0$, transitions from the tightly bound antisymmetric state B are dominated by a single excitation to the lowest-lying, most tightly bound antisymmetric state (blue peak). For $\phi = \pi/35$, mixing of left- and right-well localized states increases the number of transitions from state B , blurring the spectrum near 40 kHz. Further, the lowest final state at $E < 0$ acquires a nonzero overlap with the initial state B [blue peak at 30 kHz in Fig. 3(c)]. For transitions from the right-well state A , the strengths decrease quickly above 52 kHz, as the corresponding final states become more left-well localized with increasing energy above the fuzzy green-blue curve in Fig. 2(d).

For each initial state $i = A$ or B , we find that the sum of the Franck-Condon factors, $\sum_f |\langle f|i\rangle|^2 = 0.94\text{--}0.95$, is close to unity, using only bound state solutions [Eq. (4)]. This

appears to be a general property, arising from the radial confinement and periodic boundary conditions imposed on a lattice of finite length [16]. Hence, we can fit the spectrum using the transition probabilities of Figs. 3(a) and 3(c). As we expect the initial states to be thermally populated for the conditions of our experiment, we take the total spectrum to be proportional to $S(\nu) \propto \exp[-E_A/k_B T] S_A(\nu) + \exp[-E_B/k_B T] S_B(\nu)$. The red curves show the fits with $k_B T = 0.35 E_R$ for $\phi = 0$ and $0.43 E_R$ for $\phi = \pi/35$. An extended calculation [16], using a Boltzmann factor weighted sum over all Q , yields equally good fits, but with the same temperature, $k_B T = 0.48 E_R \simeq k_B \times 0.34 \mu\text{K}$, for both $\phi = 0$ and $\phi = \pi/35$.

From the very good agreement between our model and the data, we conclude that, for small ϕ , the spectra arise from two initially populated dimer states (for each Q), denoted $i = A, B$ in Figs. 2(a) and 2(d). We see that the symmetry of the double wells greatly affects both the strengths and the distribution of the transitions.

In summary, we have measured the radio-frequency spectra of atom pair states in a 1D superlattice with radial harmonic confinement and have developed a beyond Hubbard, multiband model, which explains the spectral structure. This model can be used to test the validity of analytic approximations and to characterize the states and populations of atom pairs in general optical lattices, providing a foundation for new experiments with strongly interacting fermions.

Primary support for this research is provided by the Division of Materials Science and Engineering, the Office of Basic Energy Sciences, Office of Science, U.S. Department of Energy (DE-SC0008646). Additional support for the JETlab atom cooling group has been provided by the Physics Divisions of the Army Research Office (W911NF-14-1-0628), the National Science Foundation (PHY-1705364) and the Air Force Office of Scientific Research (FA9550-16-1-0378).

J. K. and C. C. contributed equally to this work.

*Corresponding author.

jethoma7@ncsu.edu

- [1] T. Salger, C. Grossert, S. Kling, and M. Weitz, *Phys. Rev. Lett.* **107**, 240401 (2011).
- [2] D. Witthaut, T. Salger, S. Kling, C. Grossert, and M. Weitz, *Phys. Rev. A* **84**, 033601 (2011).
- [3] D. Pertot, A. Sheikhan, E. Cocchi, L. A. Miller, J. E. Bohn, M. Koschorreck, M. Köhl, and C. Kollath, *Phys. Rev. Lett.* **113**, 170403 (2014).
- [4] J. Li, W. Huang, B. Shteynas, S. Burchesky, F. C. Top, E. Su, J. Lee, A. O. Jamison, and W. Ketterle, *Phys. Rev. Lett.* **117**, 185301 (2016).
- [5] M. Lohse, C. Schweizer, O. Zilberberg, M. Aidelsburger, and I. Bloch, *Nat. Phys.* **12**, 350 (2016).
- [6] S. Nakajima, T. Tomita, S. Taie, T. Ichinose, H. Ozawa, L. Wang, M. Troyer, and Y. Takahashi, *Nat. Phys.* **12**, 296 (2016).
- [7] M. Kanász-Nagy, E. A. Demler, and G. Zaránd, *Phys. Rev. A* **91**, 032704 (2015).
- [8] G. Orso, L. P. Pitaevskii, S. Stringari, and M. Wouters, *Phys. Rev. Lett.* **95**, 060402 (2005).
- [9] A. T. Sommer, L. W. Cheuk, M. J. H. Ku, W. S. Bakr, and M. W. Zwierlein, *Phys. Rev. Lett.* **108**, 045302 (2012).
- [10] E. Haller, M. J. Mark, R. Hart, J. G. Danzl, L. Reichsöllner, V. Melezhik, P. Schmelcher, and H.-C. Nägerl, *Phys. Rev. Lett.* **104**, 153203 (2010).
- [11] S. Sala, G. Zürn, T. Lompe, A. N. Wenz, S. Murmann, F. Serwane, S. Jochim, and A. Saenz, *Phys. Rev. Lett.* **110**, 203202 (2013).
- [12] S. Sala and A. Saenz, *Phys. Rev. A* **94**, 022713 (2016).
- [13] J. P. Kester and L.-M. Duan, *New J. Phys.* **12**, 053016 (2010).
- [14] M. Bartenstein, A. Altmeyer, S. Riedl, R. Geursen, S. Jochim, C. Chin, J. H. Denschlag, R. Grimm, A. Simoni, E. Tiesinga *et al.*, *Phys. Rev. Lett.* **94**, 103201 (2005).
- [15] G. Zürn, T. Lompe, A. N. Wenz, S. Jochim, P. S. Julienne, and J. M. Hutson, *Phys. Rev. Lett.* **110**, 135301 (2013).
- [16] See Supplemental Material at <http://link.aps.org/supplemental/10.1103/PhysRevLett.120.083203> for details on lattice calibration, theoretical model of dimer binding in a superlattice, and its numerical implementation, which includes Refs. [17–20].
- [17] G.-B. Jo, J. Guzman, C. K. Thomas, P. Hosur, A. Vishwanath, and D. M. Stamper-Kurn, *Phys. Rev. Lett.* **108**, 045305 (2012).
- [18] K. Huang, *Statistical Mechanics* (Wiley, New York, 1963), p. 455.
- [19] I. Bloch, J. Dalibard, and W. Zwerger, *Rev. Mod. Phys.* **80**, 885 (2008).
- [20] K. Winkler, G. Thalhammer, F. Lang, R. Grimm, J. Hecker Denschlag, A. J. Daley, A. Kantian, H. P. Büchler, and P. Zoller, *Nature (London)* **441**, 853 (2006).
- [21] We assume that the effective range is negligible, which is a good approximation for the broad Feshbach resonances in ${}^6\text{Li}$.
- [22] T. Busch, B.-G. Englert, K. Rzazewski, and M. Wilkens, *Found. Phys.* **28**, 549 (1998).
- [23] Z. Idziaszek and T. Calarco, *Phys. Rev. A* **74**, 022712 (2006).
- [24] C. Cheng, J. Kangara, I. Arakelyan, and J. E. Thomas, *Phys. Rev. A* **94**, 031606 (2016).
- [25] Y. Zhang, W. Ong, I. Arakelyan, and J. E. Thomas, *Phys. Rev. Lett.* **108**, 235302 (2012).